Contents lists available at ScienceDirect

Optics Communications

5 Gbaud QPSK coherent transmission in the mid-infrared

Wei Wang [a,b,*], Yunqiang Zheng [a], Xiaoping Xie [a,b], Yulong Su [a,b], Xinning Huang [a,b], Tao Duan [a], Wei Zhao [a,b]

[a] *State Key Laboratory of Transient Optics and Photonics, Xi'an Institute of Optics and Precision Mechanics (XIOPM), Chinese Academy of Sciences (CAS), Xi'an 710119, China*
[b] *University of Chinese Academy of Sciences (UCAS), Beijing 100049, China*

ARTICLE INFO

ABSTRACT

We experimentally demonstrate a high-speed mid-infrared (MIR) transmission system with a 5 Gbaud quadrature phase shift keying (QPSK) modulation over free space optical (FSO) link. The MIR system operates through homemade robust and compact MIR transmitter and receiver devices, which has the ability to achieve wavelength conversion between C-band and MIR based on difference frequency generation (DFG) process. The wavelength and power of MIR signal generated from MIR transmitter are 3.57 dBm and 3594 nm, and the C-band signal regenerated from MIR receiver are -26.12 dBm and 1550.116 nm. Both the constellation diagrams and eye diagrams of regenerated C-band signal are clear when the input power of C-band receiver is higher than -40 dBm. Compared with the back to back (BTB) transmission system, the power penalty of the MIR transmission system is less than 2.8 dB measured at bit error ratio (BER) of 1×10^{-7}. It can be concluded from the experimental results that the MIR transmission system supports high-speed data rate, variable wavelength and high-order modulation format, and has the potential to be applied to FSO communications or satellite communications in atmospheric environments.

1. Introduction

Mid-infrared (MIR) communication over free space optical (FSO) link has gained more extensive research in recent years [1–3]. Due to advances in atmospheric transmission properties, MIR wavelengths (2 μm∼6 μm) have more transmission advantages compared with telecom-band [4]. Some experimental results show that the transmittance of 3.6 μm has a 26% increase compared to 1.55 μm in clean weather [5]. Moreover, The MIR transmission provides link stability with 2x to 3x greater transmission over 1.55 μm in adverse weather, such as mist, fog, and haze [6,7]. Hence, MIR communication is a more reliable means of FSO communication under atmospheric conditions. The availability of FSO links at NIR wavelength [8–10] has been demonstrated by many aero-space projects so far, such as Lunar Laser Communication Demonstration (LLCD) project [11,12] led by National Aeronautics and Space Administration (NASA), European Data Relay Satellite System (EDRS) project [13] led by European Space Agency (ESA). Yet, MIR communication has been hindered by lack of several core devices such as high-speed quantum-cascade lasers (QCLs) [14] and quantum-well infrared photodetectors, which makes the early MIR system operates only on the order of 10 Mbps.

Currently, MIR communication is being studied in order to achieve high-speed (> Gbps) transmission. High-speed interband cascade lasers

operating at 3 μm was demonstrated with a bandwidth of 3 GHz for low-temperature operation by Soibel et al. [15]. Martini et al. has validated a 2.5 Gbps transmission at 8 μm by using QCL at ultra-low temperature [16,17]. A pulse amplitude modulation with a data rate of 4 Gbps over free space transmission using a 4.65-μm QCL is demonstrated recently by Pang et al. [18,19]. It can be clearly seen that for direct modulation of QCLs and direct detection of photodetectors are difficult to achieve high-speed (up to 10 Gbps) MIR communication due to the bandwidth limitation, and cryogenic operation temperature also prevents QCLs being widely used at the current stage, another severely insufficient is that all studies focus only on intensity transmission. However, the MIR light sources produced by difference frequency generation (DFG) process are insensitive to the data rates and modulation formats [20–22]. Buchter et al. has developed a data-format-independent MIR transceiver at 3.8 μm region, which exploits DFG process in Ti-indiffused periodically poled LiNbO$_3$ crystal and has successfully implemented a phase modulation transmission on the order of 1 Gbps, and the receiver sensitivity is close to back to back (BTB) system [23]. Hao et al. has exploited a 3.6 μm transmitter and receiver based on DFG process with a 1.5 μm telecom source and a 1.08 μm pump laser, which has carried out a data rate of 200 Mbps transmission with a very low bit error rate (BER) over free space [24]. However,
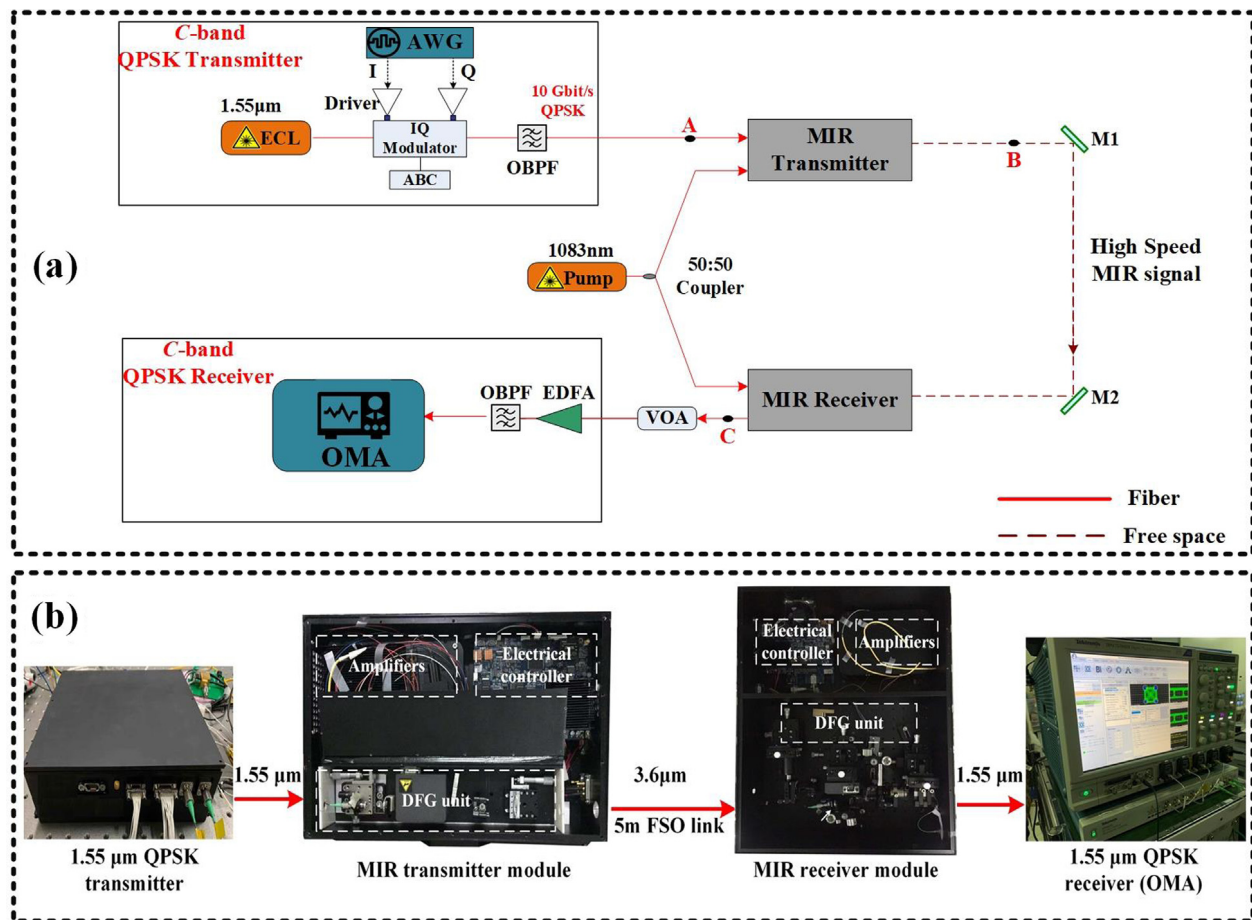
Fig. 1. (a) Schematic diagram of MIR system; (b) photographs of the all parts of MIR transmission system.

the study of ten gigabits per second speed and higher-order modulation transmission in MIR band still needs in-depth analysis.

In this paper, we build a MIR transmission system operated at 5 Gbaud (10 Gbps) with a quadrature phase shift keying (QPSK) modulation at 3.6 μm, which is a greatly improvement of our previous work of DPSK transmission [25]. In the experiment, the DFG process is generated in the nonlinear MgO-doped periodically poled LiNbO$_3$ (PPLN) crystal, which can implement wavelength conversion between 1.55 μm and 3.6 μm [26,27]. The power and wavelength of generated MIR QPSK signal are 3.57 dBm and 3594 nm with injected powers of 33 dBm and 37 dBm at 1550 nm and 1083 nm, and the regenerated QPSK signal is −26.12 dBm and 1550.116 nm with injected powers of −3 dBm and 36.5 dBm at 3594 nm and 1083 nm. When the regenerated power decreases from −35 to −45 dBm, the measured root mean square (RMS) error vector magnitude (EVM) [28] of demodulated QPSK signal increases from 11.7% to 22.4%. In the end, the power penalty of the MIR system is less than 2.8 dB compared to the BTB system, which is measured at BER of 1×10^{-7}.

2. Experiment setup

Fig. 1(a) shows the experimental setup of MIR transmission system, which mainly consists of four parts: A *C*-band QPSK transmitter, a MIR transmitter, a MIR receiver and a *C*-band QPSK receiver. The following is a detailed introduction to the four parts structure.

2.1. Configuration of C-band QPSK transmitter

As shown in Fig. 1(a), a narrow linewidth (around 5 kHz) external cavity laser (ECL, RIO0075-3-ITU-3) generates a continuous wave at

1550 nm, which is modulated by an IQ-type optical modulator with a 20 GHz 3-dB bandwidth. Two synchronous electrical signals with a data rate of 5 Gbps generated from a pulse pattern generator pattern (PPG, Tektronix AWG70002) are amplified to approximately 8 V by two radio frequency power amplifiers (IXBLUE DR-DG-10-MO-NRZ). The two data streams are set to pseudo-random bit sequence (PRBS) $2^{15}-1$ and 2^7-1 patterns, respectively. Simultaneously, three proper voltages are applied to the IQ modulator through an automatic bias control device, which make the modulator work in QPSK mode for a long time. Thereafter, an optical band pass filter (OBPF) with a gaussian shape and a 3-dB bandwidth of 0.4 nm is employed to compress the spectrum width for improving the optical signal to noise ratio (OSNR).

2.2. Configuration of MIR transmitter

Fig. 2 depicts the complete components in MIR transmitter, which has two input and one output interfaces. The main function of MIR transmitter is an implementation of DFG process. One of the input interfaces is used to connect the 1550 nm QPSK signal, and a polarization maintaining high-power amplification is designed to amplify the 1550 nm QPSK signal to 2 W by a high-power Er-Yb-doped fiber amplifier (HP-EYDFA) with internal polarization maintaining fiber. The other input interface is used to connect with a polarization maintaining ytterbium-doped fiber laser (YDFL) as a pump laser, which delivers 10 dBm linearly polarized light at 1083 nm. A 50:50 beam splitter is used to split the 1083 nm pump for MIR transmitter and receiver devices shown in Fig. 1(a). Similarly, the power of 1083 nm light is boosted to 5 W by a high-power Yb-doped fiber amplifier (HP-YDFA). Two high power isolators available for 1550 nm and 1083 nm are placed behind
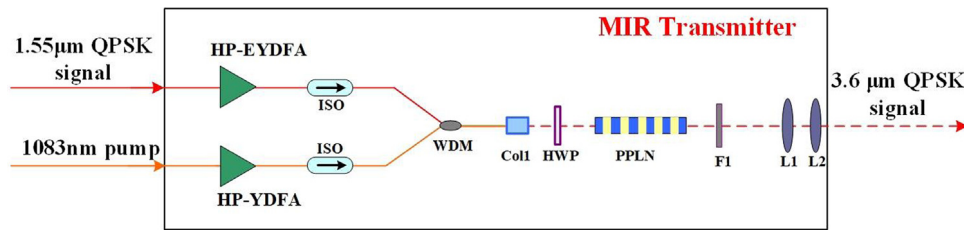
Fig. 2. MIR transmitter structure used to generate 3.6 μm QPSK signal, which is mainly based on DFG effect.
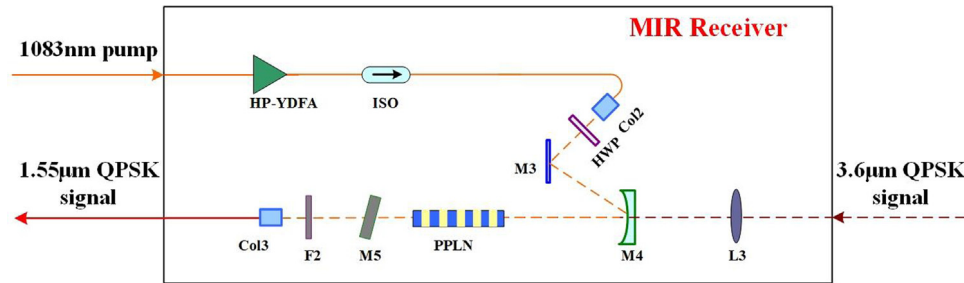

Fig. 3. MIR receiver structure used to regenerate 1.55 μm QPSK signal, which is mainly based on DFG effect.

two amplifiers, which can suppress the power of signal reflection more than 40 dB and prevent damage to amplifiers.

A specially customized high-power wavelength-division multiplexer (WDM) is used to combine the amplified two beam lights, and then the combined beam propagates into the air after collimated by an optical collimator. After passing through a half-wave plate (HWP), the beam light directly emits into the geometric center position of PPLN crystal (made by HCP) surface, and PPLN crystal has a length of 50 mm and the doping MgO concentration is 5%. The HWP can be controlled manually to adjust the polarization states of incident beams in order to minimize phase mismatch [18,19]. The residual unconverted 1550 nm and 1083 nm lights are filtered by a rectangular bandpass filter F1 with a center wavelength of 3.6 μm and a bandwidth of 0.3 μm. Two followed collimator lenses L1 and L2 used to collimate the 3.6 μm beam into a parallel light bundle are placed at the end of MIR transmitter.

2.3. Configuration of MIR receiver

Fig. 3 shows the all components of the MIR receiver. Before entering the MIR receiver, two high reflection mirrors M1 and M2 are employed to build a 10 m propagation path from transmitter to receiver shown in Fig. 1(a). The 3.6 μm signal is spatially collimated and fine-tuned the direction by a lens L3 made of silicon and germanium, and the 1083 nm pump beam out of a fiber to lens collimator Col2 is spatially coupled with the 3.6 μm signal through a mirror M4 with a flat-concave shape. The focal length of L3 and M4 are 100-mm and 50-mm, respectively. The merged beams are focused at the center of the front face of the PPLN crystal and careful alignment should be done in order to optimize the spatial overlap between signal and pump modes in the PPLN crystal. At the end of MIR receiver, a dichroic mirror M5 with a high reflection at 1083 nm and a bandpass window filter F2 with a 3-dB bandwidth of 20 nm at 1550 nm are used to remove the residual 1083 nm and 3.6 μm light in DFG light.

2.4. Configuration of C-band QPSK receiver

The schematic diagram of 1.55 μm receiver is shown in Fig. 1(a). A low noise EDFA with a noise figure of 3.8 dB and a gain greater than 45 dB is used to amplify the regenerated 1.55 μm QPSK signal. The amplified signal is filtered through a gaussian-type filter to primarily suppress amplified spontaneous emission noise and nonlinear process noise. The subsequent experimental procedure is designed to

perform QPSK signal demodulation, which is operated by a 25 GHz optical modulation analyzer (OMA, Tektronix OM4225) [29], including coherent detection, high speed electrical signal acquisition and offline digital signal processing (DSP) [30,31], as shown in Fig. 4. For offline DSP in OMA, the IQ imbalances compensation block is mainly to correct the phase and gain mismatch between *I* and *Q* ports with the Gram–Schmidt orthogonalization procedure (GSOP) [32], then multiple samples to perform timing recovery based on Gardner algorithm [33]. The frequency mismatch between transmitting laser and local oscillator (LO) laser, and the laser phase noise are estimated and compensated by frequency and phase estimation block, which mainly realized by the fast Fourier transform (FFT) algorithm and Viterbi–Viterbi algorithm, respectively.

3. Results and discussion

3.1. 5 Gbaud QPSK signal generation at 1.55 μm

Fig. 5(a) shows the optical spectrum of generated 5 Gbaud QPSK signal at 1.55 μm. The OSNR of QPSK signal is 51.1 dB measured by an optical spectrum analyzer (OSA, YOKOGAWA AQ6370), and the measured signal power and center wavelength are −1.92 dBm and 1550.112 nm, respectively. The eye diagram of 5 Gbaud QPSK is shown in Fig. 5(b), which has a clear profile and three levels are clearly observed in the bit-to-bit transition regions.

3.2. MIR QPSK signal transmission

The 1.55 μm QPSK signal is injected into the MIR transmitter with the 1083 nm pump light for MIR signal generation. The first process is the amplification of the two lasers, both the bottom of HP-EYDFA and HP-YDFA are tightly attached to the heat sink for long-term power stability. Fig. 6(a) shows the measured stabilities of two amplifiers output power by an optical power meter (OPM, JDSU OLP-55) in 35 min, the measured stable powers are 2.01 W at 1550 nm and 5.07 W at 1083 nm, respectively. The measured results show that both the output power drifts of two amplifiers in the automatic power control (APC) mode are less than 1%. It can be clearly observed that the output power of 1550 nm amplifier tends to a stable state after the amplifier is turn on for 5 min. The second process uses the coupled two amplified lasers to emit into PPLN crystal for DFG process. Fig. 6(b) shows the optical spectrum of generated DFG light through the window filter F1,
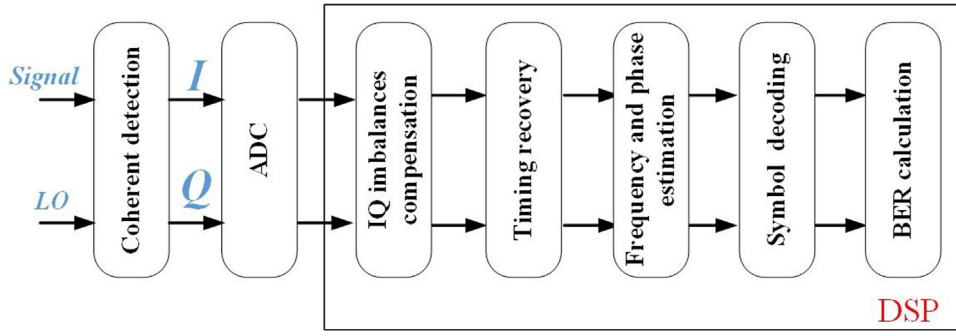
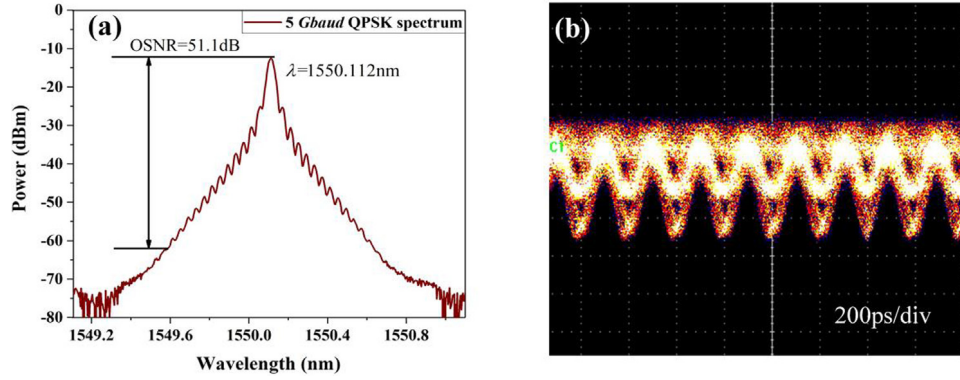**Fig. 4.** Sequence of regenerated 1.55 μm QPSK signal demodulation in the OMA.

Fig. 5. (a) The generated 5 Gbaud QPSK optical spectrum with a center wavelength of 1550.112 nm; (b) measured 5 Gbaud QPSK eye diagram.
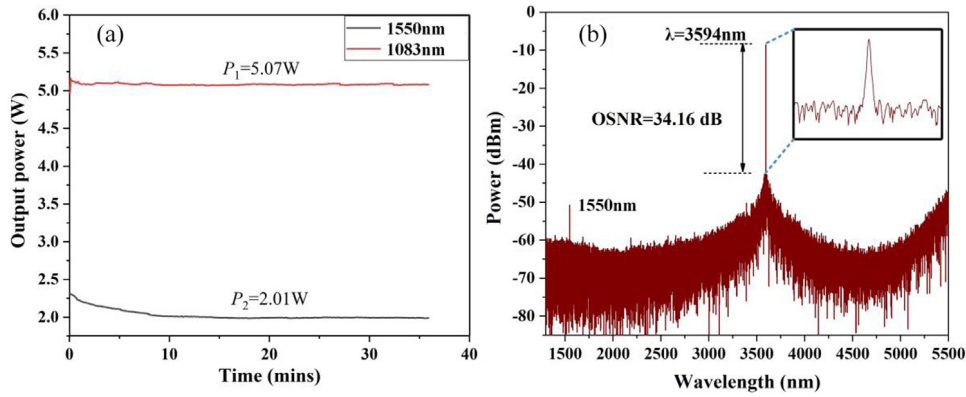

Fig. 6. (a) The measured power stability of 1550.12 nm and 1083 nm amplifiers; (b) the optical spectrum of generated DFG light through the window filter F1.

and it can be noted that there is a very significant MIR signal and a very weak residual 1550 nm signal in the optical spectrum. The MIR signal has a good OSNR about 34.16 dB and the measured power and center wavelength of MIR signal are 3.57 dBm and 3594 nm.

The power of generated MIR signal depends on conversion efficiency in nonlinear DFG process, which can usually be expressed mathematically as [34–36]:

$$\eta_{DFG} \propto \frac{\lambda_s}{\lambda_i} L^2 P_P(0) \sin c^2(\frac{\Delta\beta_{DFG}L}{2}) \tag{1}$$

where λ_s, λ_p and λ_i are the wavelength of signal, pump and idler wave $(1/\lambda_i = 1/\lambda_p - 1/\lambda_s)$, L is the device geometry of PPLN crystal, $P_P(0)$ is the pump power and $\Delta\beta_{DFG}$ is the phase mismatch term. The above parameters have been fixed, except that the term $\Delta\beta_{DFG}$ can be adjusted, which is closely related to the temperature of PPLN crystal. To achieve minimum phase mismatch in the DFG process, the PPLN crystal surfaces are covered with thermal insulation films and the surrounding temperature is controlled within ±0.1 °C. Fig. 7 shows the obtained MIR

signal powers versus the temperature of thermoelectric cooler (TEC) attached to the surface of PPLN crystal in simulation and experiment. In the experiment, the optimum temperature of conversion efficiency is measured to be 53.02 °C for a PPLN crystal with a grating period of 30 μm. As the temperature increases from 42.2 to 53.02 °C, the generated normalized MIR signal power increases rapidly from 0.22 to 0.94. Moreover, the optimum temperature in numerical calculations is 50.4 °C, which is close to the experimental results with a deviation of 2.62 °C. The deviation between simulation and experiment results may be due to the spatial aberration of the optical modes from the simple approximation of plane waves.

The MIR signal and 1083 nm pump lights entering the MIR receiver are adjusted the direction to achieve accurate coaxiality and spatial merging by the mirror M3 and M4 shown in Fig. 3, and the power of two waves incident on the front face of the PPLN crystal are 4.7 W (36.5 dBm) and 0.5 mW (−3 dBm). DFG light is generated with the accurate temperature and polarization state matching of PPLN crystal,
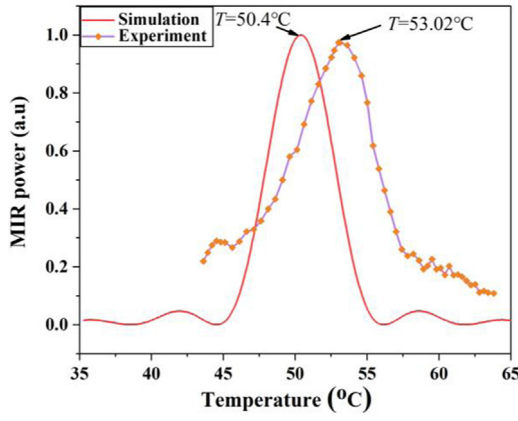
Fig. 7. Simulation and experimental results of the MIR QPSK signal power versus the operation temperature of the PPLN crystal.
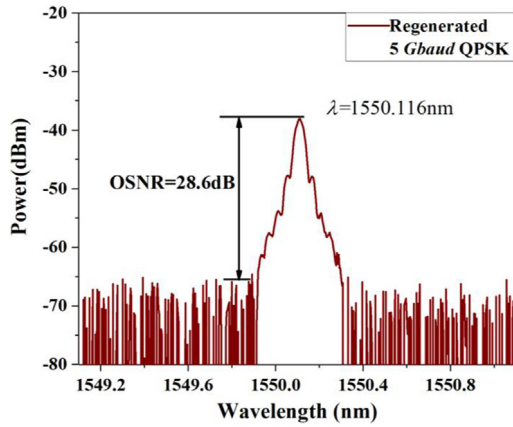

Fig. 8. The measured regenerated QPSK signal spectrum.

and is spectrally selected out by the mirror M5 with a 99.5% reflectivity at 1083 nm and a 99.5% transmittance at 1550 nm. The rectangular bandpass filter F2 is used to remove the residual broadband amplified spontaneous emission noise, which can improve the OSNR of regenerated signal. The measured regenerated 1550 nm QPSK signal power and

wavelength is −26.12 dBm and 1550.116 nm, as shown in Fig. 8. It can be observed that equally spaced sidebands are still remained on both sides of the regenerated signal spectrum, which can match the original 1.55 μm signal spectrum well shown in Fig. 5(a), and the wavelength deviation is only 0.004 nm. Here, the conversion efficiency is calculated in order to characterize the system capabilities. At the MIR transmitter, the power of input 1.55 μm signal and the output 3.6 μm signal power are 33 dBm and 3.57 dBm, so the conversion efficiency of the MIR transmitter is about 1.14%. At the MIR receiver, the power of input 3.6 μm signal and the output 1.55 μm signal power are −3 dBm and −26.12 dBm, so the conversion efficiency of the MIR receiver is about 4.7%.

3.3. Regenerated 1.55 μm QPSK signal demodulation

The commercial lens to fiber coupler Col3 couples the regenerated signal into an optical fiber with a 6.8 dB power loss. At the *C*-band receiver, the power of regenerated QPSK signal is amplified to 20 dBm by an EDFA. and the remaining power through Gaussian filter is 5.41 dBm. Then the signal is sent into the OMA to perform QPSK demodulation. The OMA is configured in single-polarization QPSK demodulation mode, the wavelength and output power of the built-in LO laser are set to 1550.116 nm and 16 dBm. The following process includes coherent detection, electrical signals digital sampling with a sample rate of 25 GSa/s and DSP processing. Fig. 9(a) shows the original constellation diagram without the DSP algorithm, which is very disorderly and has a circular shape. Fig. 9(b)–(d) are the recovery four phase-states constellation diagrams by using DSP algorithm, which correspond to input powers of −35, −40 and −45 dBm. The successful demodulation of regenerated 5 Gbaud QPSK signal means that *C*-band-MIR-*C*-band conversion still retains all phase and amplitude information. The calculated root mean square (RMS) error vector magnitude (EVM) of three constellations are 11.7%, 15.5% and 22.4%, respectively. Fig. 9(e)–(j) show the I and Q eye diagrams of each constellation, the measured average Q-factor are 7.1, 5.5 and 3.6 in Fig. 9(e)–(g), and it can be clearly seen that when the received power is higher than −40 dBm, the opening of eye diagram is better.

In order to further evaluate the performance of the MIR transmission system, several parameters of the MIR system and BTB system are compared experimentally. To make the input conditions are the same, the input power of *C*-band receiver can be adjusted in the range of −35 to −45 dBm by controlling the VOA. Fig. 10(a) illustrates the EVM results versus the received power in MIR and BTB system. With
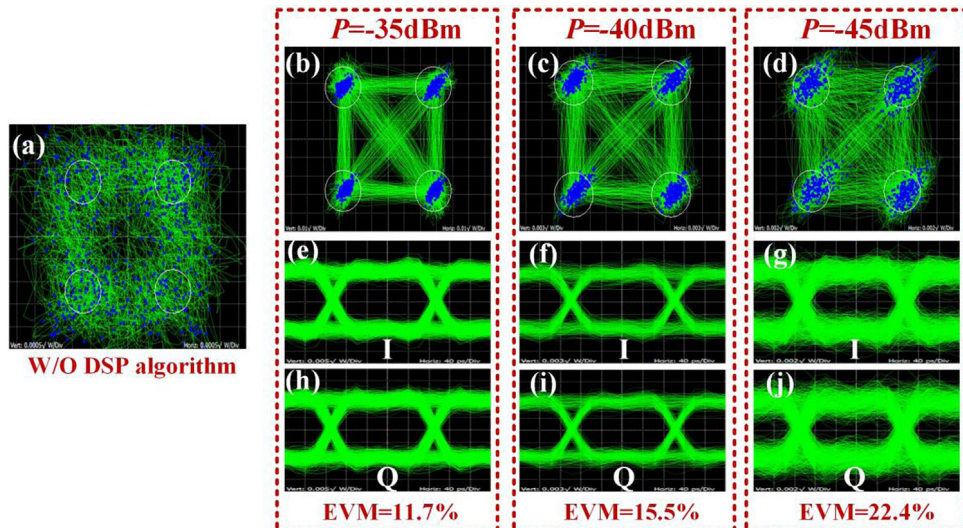

Fig. 9. The measured constellation diagrams for: (a) without DSP algorithm; (b) received power of −35 dBm; (c) received power of −40 dBm; (d) received power of −45 dBm; (e)–(j) I and Q eye diagrams.
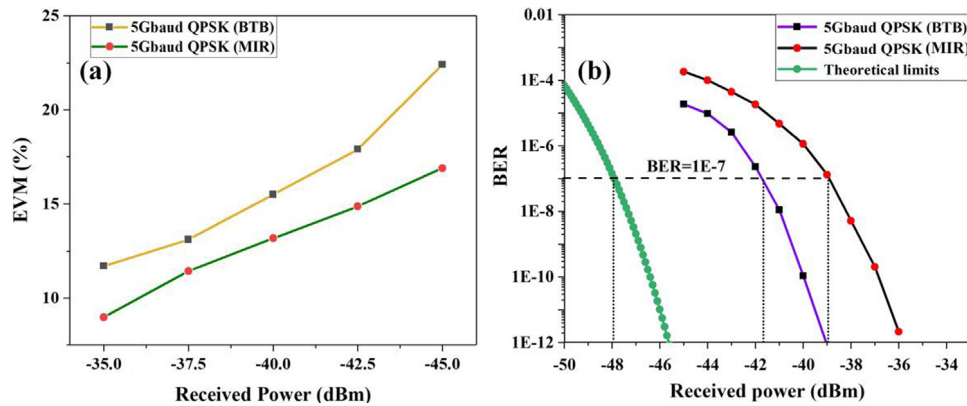
Fig. 10. Performance comparison of MIR and BTB transmission systems for: (a) EVMs versus received power; (b) BERs versus received power.

the received power decreases from −35 to −45 dBm, the measured EVMs in MIR system and BTB system are distributed in the range of 11.7% to 22.4% and 9% to 17.2%. Correspondingly, about 2.7% to 5.2% EVM loss will arise from −35 to −45 dBm, which means that as the received power is lower, the EVM loss is higher. Finally, the theoretical and measured receiver sensitivities are used to evaluate and compare two systems. The BERs are plotted as functions of the received power, as shown in Fig. 10(b). The measured required powers are −38.85 dBm and −41.58 dBm for the MIR system and BTB system at BER of 1×10^{-7}, and the theoretical limit is −47.82 dBm at BER of 1×10^{-7}. Hence, the power penalty between MIR system and BTB system, theoretical limit are 2.73 dB and 8.97 dB at BER of 1×10^{-7}, respectively.

4. Conclusions

In conclusion, we present a DFG-based high-speed MIR transmission system over 10 m FSO link by using wavelength conversion between C-band and MIR. The wavelength of 5 Gbaud QPSK signal is converted through *C*-band-MIR-*C*-band, but all phase and amplitude information are still retained in experiment. The wavelength and power of MIR signal generated from MIR transmitter are 3.57 dBm and 3594 nm, and the *C*-band signal regenerated from the MIR receiver are −26.12 dBm and 1550.116 nm. The power penalty of the MIR system is less than 2.8 dB compared to the BTB system, which is measured at BER of 1×10^{-7}. This experiment can provide valuable reference for future high-speed and high-order modulation communication in the MIR.

Acknowledgments

References

[1] M. Grabner, V. Kvicera, J. Lightwave Technol. 32 (3) (2014) 513–520.
[2] C.P. Colvero, M.C.R. Cordeiro, J.P.V. Weid, Electron. Lett. 41 (2005) 610.
[3] V.W.S. Chan, J. Lightwave Technol. 24 (12) (2006) 4750–4762.
[4] T. Plank, E. Leitgeb, P. Pezzei, Z. Ghassemlooy, 17th European Conference on Networks and Optical Communications, Spain, 2012, pp. 1–5.
[5] A. Arnulf, J. Bricard, E. Curé, C. Véret, J. Opt. Soc. Amer. 47 (6) (1957) 491–498.
[6] P. Corrigan, R. Martini, E.A. Whittaker, C. Bethea, Opt. Express 17 (6) (2009) 4355–4359.
[7] A. Soibel, M.W. Wright, W.H. Farr, S.A. Keo, C.J. Hill, R.Q. Yang, H.C. Liu, IEEE Photonics Technol. Lett. 22 (2) (2010) 121–123.
[8] B. Janjua, T.K. Ng, C. Zhao, H.M. Oubei, C. Shen, A. Prabaswara, M.S. Alias, A.A. Alhamoud, A.A. Alatawi, A.M. Albadri, A.Y. Alyamani, M.M. El-Desouki, B.S. Ooi, Opt. Express 24 (17) (2016) 19228–19236.
[9] J.R.D. Retamal, H.M. Oubei, B. Janjua, Y.C. Chi, H.Y. Wang, C.T. Tsai, T.K. Ng, D.H. Hsieh, H.C. Kuo, M.S. Alouini, J.H. He, G.R. Lin, B.S. Ooi, Opt. Express 23 (26) (2015) 33656–33666.
[10] D.J. Israel, B.L. Edwards, J.W. Staren, 2017 IEEE Aerospace Conference, 2017, pp. 1–6.
[11] A. Biswas, J.M. Kovalik, M.W. Wright, W.T. Roberts, M.K. Cheng, K.J. Quirk, M. Srinivasan, M.D. Shaw, K.M. Birnbaum, Free-Space Laser Communication and Atmospheric Propagation XXVI, Vol. 8971, 2014, p. 89710X.
[12] B.L. Edwards, B. Robinson, A. Biswas, J. Hamkins, 2015 IEEE International Conference on Space Optical Systems and Applications (ICSOS), 2015, pp. 1–8.
[13] M. Gregory, F.F. Heine, H. Kämpfner, R. Lange, M. Lutzer, R. Meyer, Opt. Eng. 51 (3) (2012) 031202.
[14] V. Raghunathan, D. Borlaug, R.R. Rice, B. Jalali, Opt. Express 15 (22) (2007) 14355–14362.
[15] A. Soibel, M. Wright, W. Farr, S. Keo, C. Hill, R.Q. Yang, H.C. Liu, Free-Space Laser Communication Technologies XXII, in: Proc. SPIE, vol. 7587, 2010, p. 75870S.
[16] R. Martini, R. Paiella, C. Gmachl, F. Capasso, E.A. Whittaker, H.C. Liu, H.Y. Hwang, D.L. Sivco, J.N. Baillargeon, A.Y. Cho, Electron. Lett. 37 (21) (2001) 1290.
[17] R. Martini, C. Gmachl, J. Falciglia, F.G. Curti, C.G. Bethea, F. Capasso, E. Whittaker, R. Paiella, A. Tredicucci, A. Hutchinson, D.L. Sivco, A.Y. Cho, Electron. Lett. 37 (3) (2001) 191.
[18] X.D. Pang, O. Ozolins, L. Zhang, R. Schatz, A. Udalcovs, J. Storck, G. Maisons, M. Carras, S. Xiao, G. Jacobsen, S. Popov, J. Chen, S. Lourdudoss, 2017 European Conference on Optical Communication (ECOC), IEEE, 2017.
[19] X.D. Pang, O. Ozolins, R. Schatz, J. Storck, A. Udalcovs, J.R. Navarro, A. Kakkar, G. Maisons, M. Carras, G. Jacobsen, S. Popov, S. Lourdudoss, Opt. Lett. 42 (18) (2017) 3646–3649.
[20] M.A. Belki, F. Capasso, A. Belyanin, D.L. Sivco, A.Y. Cho, D.C. Oakley, C.J. Vineis, G.W. Turner, Nat. Photonics 1 (5) (2007) 288–292.
[21] M.A. Belkin, F. Capasso, F. Xie, A. Belyanin, M. Fischer, A. Wittmann, J. Faist, Appl. Phys. Lett. 92 (2008) 201101.
[22] J.W. Zhang, Z. Dong, J.J. Yu, N. Chi, L. Tao, X.Y. Li, Y.F. Shao, Opt. Lett. 37 (19) (2012) 4050–4052.
[23] K.D. Büchter, H. Herrmann, C. Langrock, M.M. Fejer, W. Sohler, Opt. Lett. 34 (4) (2009) 470–472.
[24] Q. Hao, G. Zhu, S. Yang, K. Yang, T. Duan, X. Xie, K. Huang, H. Zeng, Appl. Opt. 56 (8) (2017) 2260–2264.
[25] Y.L. Su, W. Wang, X.H. Hu, H. Hui, X.N. Huang, Y.S. Wang, J.H. Si, X.P. Xie, Biao Han, H. Feng, Q. Hao, G.S. Zhu, T. Duan, W. Zhao, Opt. Express 26 (26) (2018) 34515–34528.
[26] A.V. Okishev, J.D. Zuegel, Opt. Express 14 (25) (2006) 12169–12173.
[27] N. Leindecker, A. Marandi, R.L. Byer, K.L. Vodopyanov, Opt. Express 19 (7) (2011) 6296–6302.
[28] R. Schmogrow, B. Nebendahl, M. Winter, A. Josten, D. Hillerkuss, S. Koenig, J. Meyer, M. Dreschmann, M. Huebner, C. Koos, J. Becker, W. Freude, J. Leuthold, IEEE Photonics Technol. Lett. 24 (1) (2011) 61–63.
[29] E. Ip, A. Lau, D. Barros, J. Kahn, Opt. Express 16 (2) (2018) 753–791.
[30] T.M. Hoang, M.M. Osman, M. Chagnon, M. Qiu, D. Patel, M. Sowailem, X. Xu, D. Plant, Opt. Commun. 356 (2015) 269–277.
[31] Z.X. Yu, R.J. Cai, Z.H. Wu, H.W. He, H.X. Jiang, X.L. Feng, A.R. Zheng, J.F. Chen, S.M. Gao, Opt. Commun. 454 (2020) 124520.
[32] F.Y. Ling, D. Manolakis, J. Proakis, IEEE Trans. Acoust. Speech Signal Process. 34 (4) (1986) 829–836.
[33] F. Gardner, IEEE Trans. Commun. 34 (5) (1986) 423–429.
[34] R.L. Sutherland, D.G. Mclean, S. Kirkpatrick, Handbook of Nonlinear Optics, Marcel Dekker, 2003, Chap. 2.
[35] X.P. Liu, R.M.O. Jr, Y.A. Vlasov, W.M.J. Green, Nat. Photonics 4 (2010) 557–560.
[36] N. Chiodo, F.D. Burck, J. Hrabina, Y. Candela, J.P. Wallerand, O. Acef, Opt. Commun. 311 (2013) 239–244.